ORNL/TM-2024/3349

UO_2–Liquid Metal Suspension Fuel Concept: Alloy Selection and Depletion Calculations

Ian Greenquist
Marie Romedenne

April 2024

OAK RIDGE National Laboratory

ORNL IS MANAGED BY UT-BATTELLE LLC FOR THE US DEPARTMENT OF ENERGY

ORNL/TM-2024/3349

Nuclear Energy and Fuel Cycle Division

UO_2–LIQUID METAL SUSPENSION FUEL CONCEPT: ALLOY SELECTION AND DEPLETION CALCULATIONS

Ian Greenquist
Marie Romedenne

April 2024

Prepared by
OAK RIDGE NATIONAL LABORATORY
Oak Ridge, TN 37831
managed by
UT-BATTELLE LLC
for the
US DEPARTMENT OF ENERGY
under contract DE-AC05-00OR22725

CONTENTS

ABSTRACT

A novel nuclear fuel was recently proposed that consists of UO_2 particles suspended in a liquid metal mixture. Two liquid metal candidates were identified: BiPbSn and PbSn. Scoping simulations were performed on an over-simplified reactor core that showed a potential limit on achievable burnup. Those findings led to two questions that needed to be addressed: What is the corrosion behavior of the liquid metals toward Zircaloy-4 (Zr4)? And what level of burnup can the fuel be expected to achieve? This report documents efforts to answer both of those questions. First, corrosion experiments were performed between the liquid metal candidates and Zr4 coupons. Second, the previous scoping simulations were expanded to include depletion analyses so that maximum burnups could be estimated.

At 400°C, neither PbSn nor BiPbSn caused significant corrosion to the Zr4 coupons. At 600°C, BiPbSn did not cause significant corrosion, but PbSn did. In addition, pure bismuth and pure tin were both highly corrosive, whereas pure lead was non-corrosive. The depletion simulations found that low-enriched fuel could maintain light-water reactor operating temperatures but achieve a burnup of only about one-third of existing reactors. Higher enrichments could achieve burnups equal to or higher than those of existing reactors but at the expense of higher operating temperatures.

1. INTRODUCTION

The US Energy Information Administration predicts that wind and solar energy will outcompete nuclear energy through 2050 because of their lower manufacturing costs and government subsidies [1]. This will result in the continued decline in nuclear energy capacity in the United States. Cost-cutting innovations are needed to keep nuclear energy relevant in the coming decades. However, a major barrier to such innovations is the high cost and long timeframe of licensing materials for use in nuclear reactors. In 2019, Alloy 617 became the first new material added to the Boiler and Pressure Vessel Code in over 30 years after a 12-year, $15 million campaign [2]. These campaigns are needed to understand the effects of irradiation damage in solids and fission product–induced performance degradation in fuels. Reducing the time and cost of licensing new solid materials is an area of ongoing research [3].

Partially because of the cost and time involved in the evaluation of new structural materials, current reactor design in the United States is generally proceeding along two paths [4]. The first path is the development of next-generation light-water reactors (LWRs)—dubbed *Generation III+ reactors*—that use the same structural materials as those of existing LWRs. The second path is finishing the development of previously abandoned non-LWR concepts—*Generation IV reactors* [5].

However, a third path exists that has not been adequately explored: that of developing novel concepts using existing solid materials. This path provides an opportunity to prioritize passive safety and low costs from the inception of a reactor concept. In an effort to explore this space, Oak Ridge National Laboratory recently proposed a novel fuel form that is chemically compatible with LWR structural materials and water at LWR operating temperatures, includes no new solid materials, and has a higher thermal conductivity than sintered UO_2 pellets [6]. The fuel is a UO_2–liquid metal suspension (ULIMES), which consists of bare UO_2 particles suspended in a liquid metal. The small size of the particles and the high thermal conductivity of liquid metals can dramatically improve the overall thermal conductivity of the system, which can improve fuel performance during off-normal events such as loss-of-coolant accidents. In addition, compared to sintered UO_2 pellets, the ULIMES form mitigates concerns about high-burnup fuel degradation effects such as high burnup structure and fuel pulverization.

Previous work consisted of a concept description, literature review, and scoping calculations. To avoid making premature design decisions, it is assumed that ULIMES can come into contact with any standard

LWR material (i.e., UO_2, water, Zircaloy, stainless steel, and concrete) while in the reactor. However, the literature review found experimental evidence that the candidate liquid metals are unlikely to react with any material other than Zircaloy. This raises the question of which liquid metal mixture(s) has an acceptably low corrosion rate. The scoping calculations showed that the fuel could maintain criticality and can be controlled through water boiling. However, initial estimates put the maximum achievable burnup around 4.9 $GWd \cdot MTU^{-1}$. This raised another question: what level of burnup can the fuel reach while maintaining criticality?

This report documents two efforts undertaken to answer those two questions. Section 2 describes corrosion experiments that were performed between Zircaloy-4 (Zr4) and two liquid metal mixture candidates as well as single-component liquid metals. Section 3 describes multiphysics depletion simulations performed to predict the peak achievable burnup in several operating regimes. Section 4 then provides summaries, conclusions, and recommendations for future work.

2. CORROSION EXPERIMENTS

2.1 EXPERIMENTAL PROCEDURE

2.1.1 Fuel rod material and liquid metals

The compatibility of Zr4 (composition in Table 1) with the two candidate liquid metals—static liquid Pb62wt.%Sn (hereinafter referred to as *PbSn*) and static liquid BiPbSn (equal parts in weight)—was investigated.

Table 1. Composition of Zr4 (in wt.%) analyzed by inductively coupled plasma–optical emission spectrometry (ICP-OES) and combustion analysis for carbon.

Zr4 (Wt.%)	Sn	Fe	Cr	H	Ca	N	C	O	Hf
Bal	1.63	0.22	0.094	0.0012	0.001	0.004	0.014	0.15	0.0027

Zircaloy-4 coupons (20 × 10 × 1.5 mm) were machined from a rolled, beta-quenched and alpha-annealed Zr4 plate in the fully recrystallized state provided by ATI. Before exposures, the specimens were polished to a 600-grit surface finish, cleaned in ethanol. The metal shots (99.999 % purity) were purchased from ESPI Metals, Beantown Chemical, and Summus Industries for lead, tin, and bismuth, respectively.

2.1.2 Static Testing

Each specimen was attached to a molybdenum end cap using molybdenum wire. The end cap was then electron beam welded to a molybdenum capsule body (3 in. or 76.2 mm tall and 1 in. or 25.4 mm outer diameter). The capsules were pre-cleaned in hydrofluoric acid and were inserted into an argon-filled glove box with impurity levels ≤1 ppm O_2 and H_2O to prevent the primary molybdenum capsule from oxidizing. Each capsule was filled with solid metal shots (Table 2) to maintain a constant surface of specimen over volume of liquid metal constant between each experiment. End caps of the capsules were sealed to the capsule body using electron beam welding. As a safety measure, each capsule was then inserted in an evacuated type 316 stainless-steel capsule. A schematic representation of the capsule is given in Figure 1.

Table 2. Summary of static liquid metal exposures

Capsule number	Liquid metal / amount (g)	Temperature (°C)	Duration (h)
1	**Bi** / 170g	600	1,000
2	**Sn** / 118g	600	1,000
3	**Pb** / 170g	600	1,000
4	**BiPbSn**/Pb-50g Bi-50g Sn-50g	600	1,000
5	**PbSn**/Pb-50g Sn-82g	600	1,000
6	**BiPbSn**/Pb-50g Bi-50g Sn-50g	400	1,000
7	**PbSn**/Pb-50g Sn-82g	400	1,000

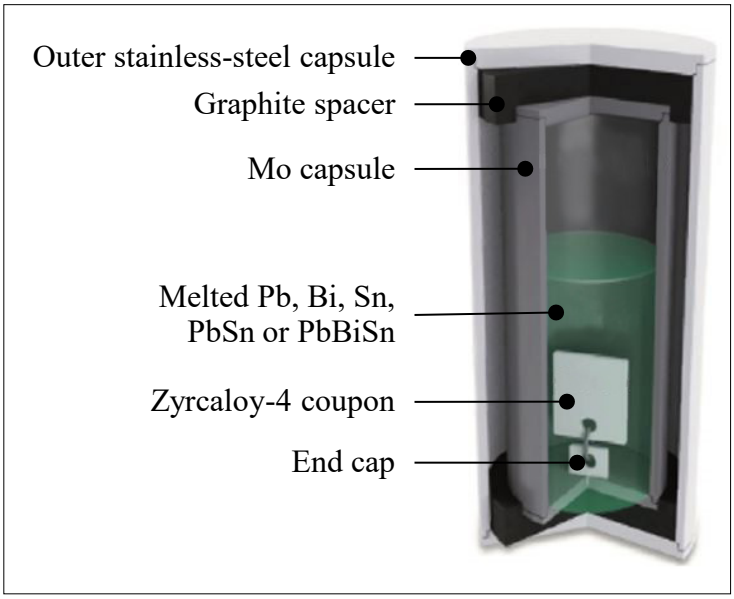

Figure 1. Schematic representation of the sealed inner molybdenum and outer stainless-steel capsules containing one Zr4 coupon and melted metal.

Exposures were performed in a box furnace at two temperatures, 400 °C and 600 °C, for 1,000 h (Table 2) in lead, tin, bismuth, PbSn and BiPbSn liquid metals. Pure liquid metal elements were investigated at 600 °C to highlight the role of liquid metal composition on compatibility. The liquid metals were not purified from oxygen using hot getter foils because Zr4 is designed to be exposed to oxygen from water and UO_2 fuel during reactor operation. Before cooling, the capsules were inverted to allow the liquid metals to drain away from the specimens, and then they were opened on the wire end in the glove box. To mitigate environmental, health and safety concerns, the samples were sequentially cleaned of residual lead and bismuth prior to handling using first a mixture of acetic acid, hydrogen peroxide (30% solution), and ethanol in a 1:1:1 solution for 72 h. To remove lead and bismuth eventually embedded in tin, the specimens were immersed in melted lithium at about 200 °C for less than 60 min. The specimen exposed

to liquid tin was not cleaned in melted lithium; this choice was made to allow the observation of potential intermetallics formed between the Zr4 coupon and tin. The potential formation of intermetallics between lead, bismuth, and Zircaloy specimens could not be observed due to the mandatory cleaning of the specimens with liquid lithium for health and safety reasons.

2.1.3 Characterization

Specimens were weighed before and after exposure using a Mettler Toledo XP205 balance with an accuracy of ±0.04 mg. Polished specimen cross sections were initially characterized using a macroscope (Keyence VR-3000 series). Secondary electron (SE) and backscattered electron (BSE) images were subsequently taken using a scanning electron microscope (ZEISS Gemini 460 SEM) equipped with energy dispersive x-ray spectroscopy (EDS). Electron backscatter diffraction (EBSD) was employed on a TESCAN MIRA3 SEM equipped with an EDAX Velocity Plus EBSD camera and the TEAM EBSD software package from EDAX. Thermodynamic calculations were performed using the ThermoCalc 2023b software and TCFE9 database.

2.2 RESULTS

2.2.1 Zircaloy-4 Microstructure before Exposure

Figure 2 shows BSE and EDS elemental maps along with EBSD Euler maps of the Zr4 microstructure before exposure. As shown in Figure 2a, Zr4 specimens consist of zirconium matrix and iron-, chromium-rich Laves phase. According to thermodynamic calculations, the alloy consists of 99 vol.% of hexagonal (HCP) zirconium and 1 vol.% $(Fe, Cr)_2Zr$ C15 Laves phase. A grain size of about 10 µm was measured using EBSD (Figure 2b).

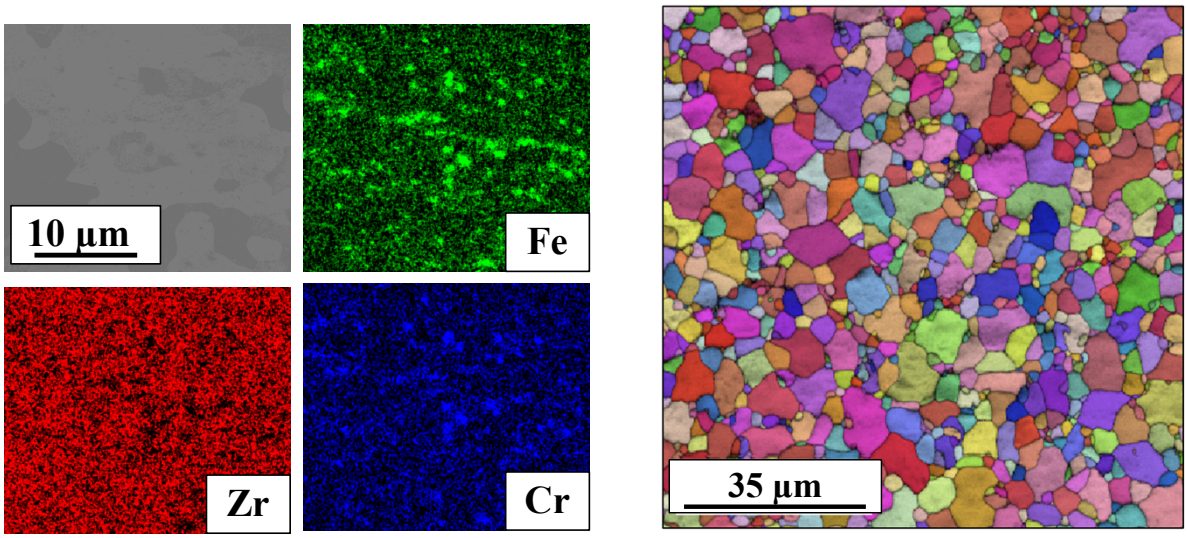

Figure 2. (a) BSE image and EDS elemental maps and (b) EBSD Euler maps of Zr4 microstructure before exposure.

2.2.2 Mass Change after Exposure

Figure 3 shows Zr4 specimen mass change per unit of area after 1,000 h of exposure in the various liquid metals at 400 and 600 °C. Mass losses were measured for Zr4 specimens after 1,000 h in static PbSn (−0.04 mg·cm^{-2}) and static BiPbSn (−0.02 mg·cm^{-2}) at 400 °C (Figure 3a). At 600 °C, complete dissolution of the specimen occurred in PbSn after cleaning in liquid lithium, which corresponded to a mass loss of 418.2 mg·cm^{-2} (Figure 3b). Mass gain was observed in BiPbSn after 1,000 h at 600 °C (+ 5.21 mg·cm^{-2}) in Figure 3b, suggesting alloying between the liquid metal and the Zr4 specimen. Finally, almost complete dissolution was observed in pure bismuth (−376.5 mg·cm^{-2}); very high mass gain was measured in pure tin (572.9 mg·cm^{-2}); and mass gain was measured in pure lead (3.92 mg·cm^{-2}), suggesting alloying between the liquid metal and the Zr4 specimen.

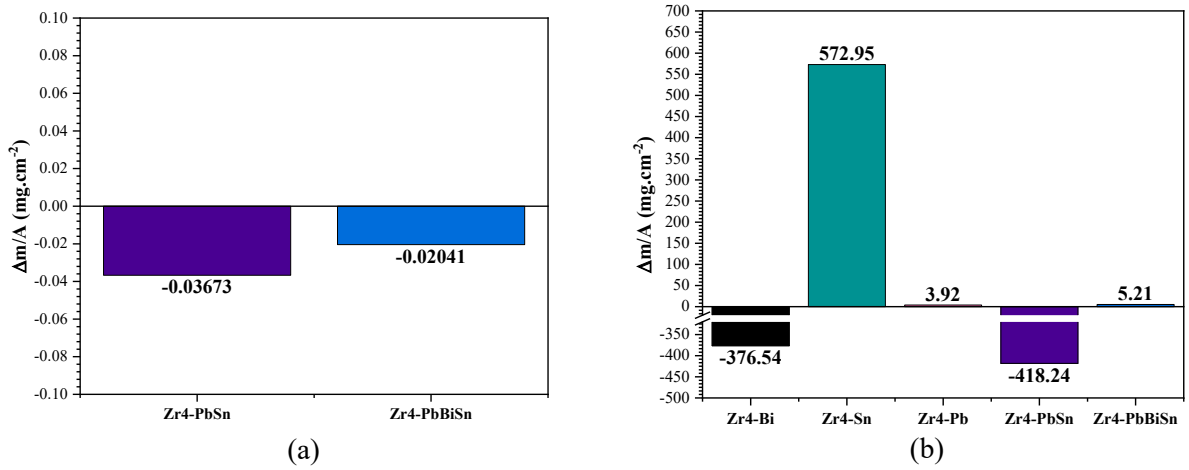

Figure 3. Specimen mass change per unit of area after 1,000 h exposure at (a) 400 °C in static PbSn and BiPbSn and (b) 600 °C in Bi, Sn, Pb, PbSn and BiPbSn after the two cleaning steps.

2.2.3 Macroscopic Observation of the Zircaloy-4 Specimens after Exposure

400 °C Exposures:

Figure 4 shows minimal degradation of the Zr4 specimens after 1,000 h of exposure in both PbSn and BiPbSn, which is in agreement with the low mass changes measured, as shown in Figure 3a.

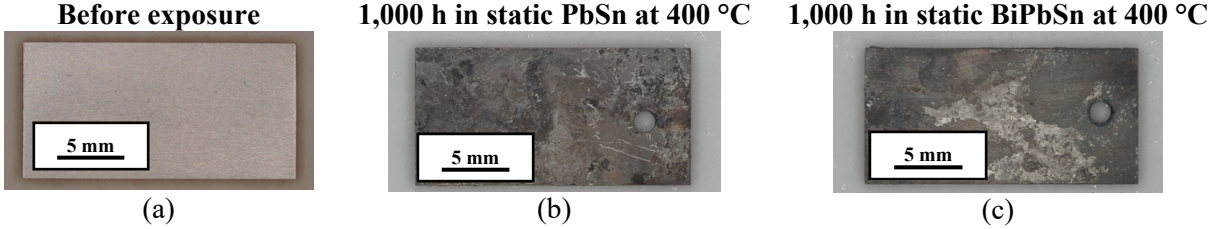

Figure 4. Keyence images of Zr4 specimen (a) before exposure, (b) after 1,000 h in static PbSn at 400 °C, and (c) after 1,000 h in static BiPbSn at 400 °C.

Figure 5 shows BSE images and associated EDS line scans of Zr4 specimens after 1,000 h of exposure in both PbSn and BiPbSn at 400 °C. ZrO_2 oxides (0.7 ± 0.1 µm thick) formed on the surface of both specimens (Figure 5). In addition, about 10 at.% oxygen was measured in the underlying alloy.

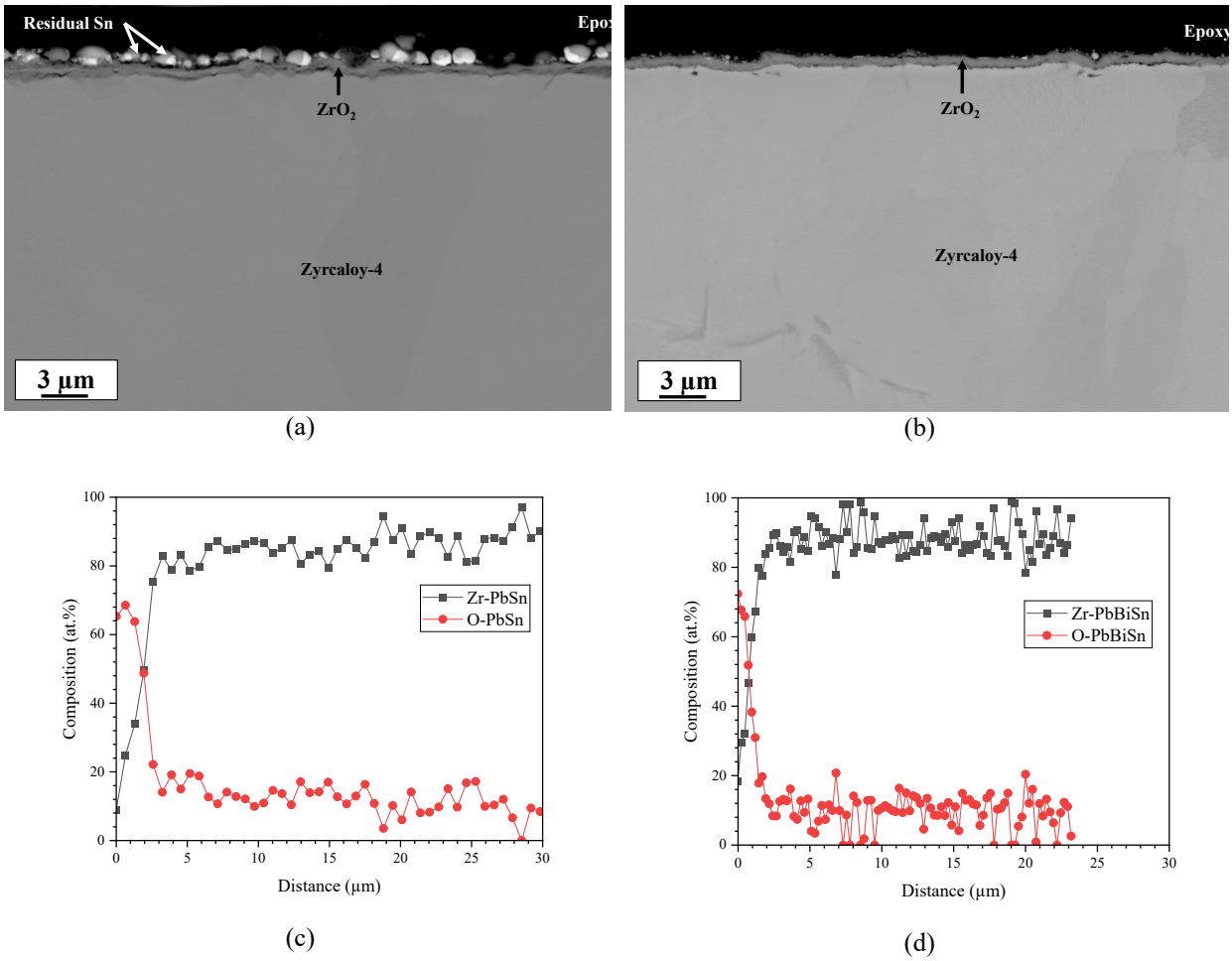

Figure 5. BSE images and EDS line scans of Zr4 specimens after 1,000 h in (a, c) PbSn and (b, d) BiPbSn at 400 °C.

In Figure 6, EDS elemental maps show the presence of the zirconium-rich oxide along with the residual tin on the surface of both specimens.

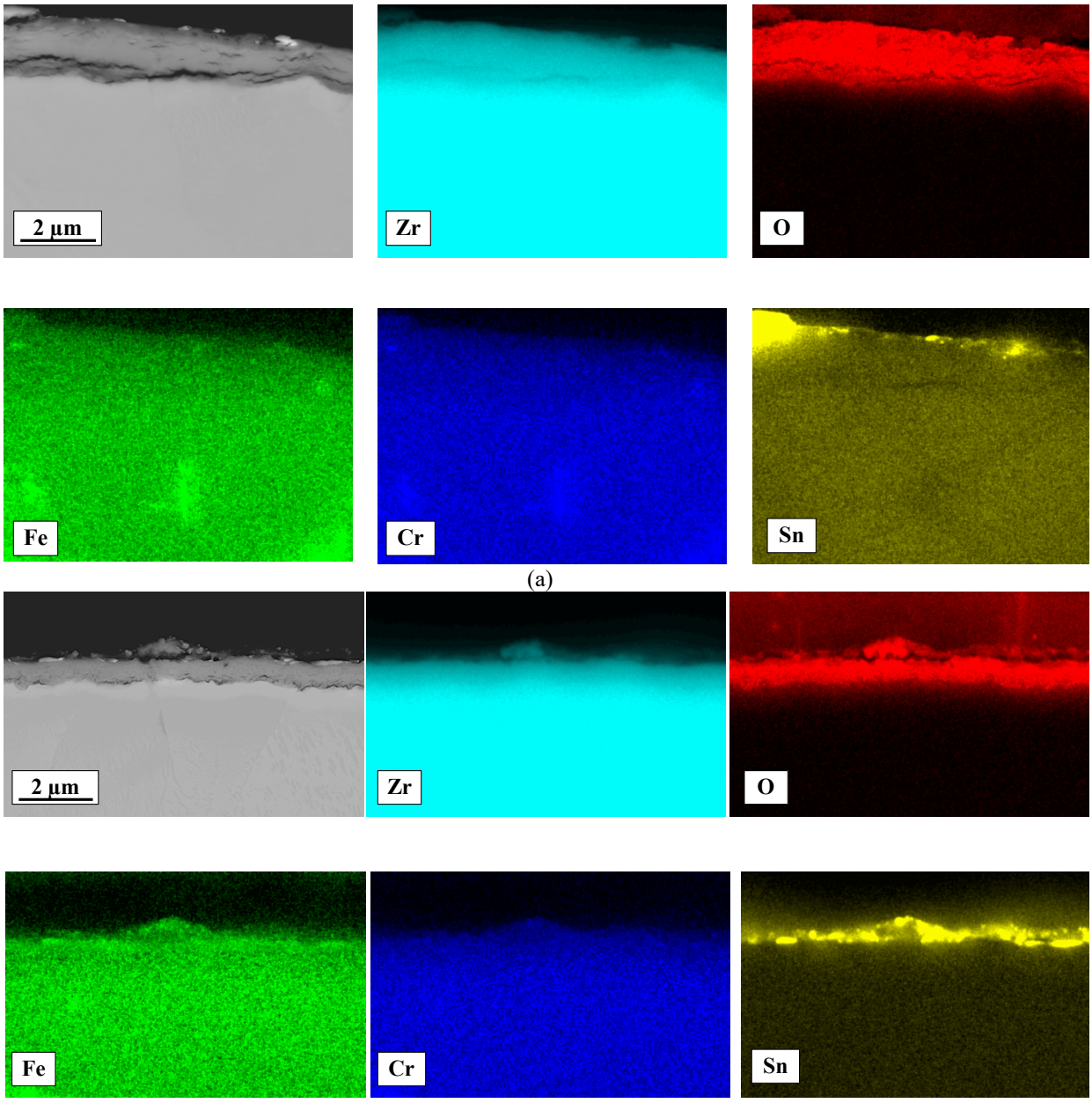

Figure 6. EDS elemental maps of Zr4 specimens after 1,000 h in static (a) PbSn and (b) BiPbSn at 400 °C.

600°C Exposures:

Figure 7 shows macroscopic images of the Zr4 specimens after 1,000 h of exposure to static PbSn and BiPbSn at 600 °C. After the first cleaning step, the Zr4 specimens were still covered by the metallic liquid metals (Figure 7b and c). After cleaning in liquid lithium at 200 °C to remove residual tin, the Zr4 specimen exposed in PbSn could not be recovered, which suggested complete degradation of the specimen after 1,000 h at 600 °C (Figure 7d). The Zr4 specimen was recovered after being exposed in liquid BiPbSn and cleaning in liquid lithium (Figure 7e).

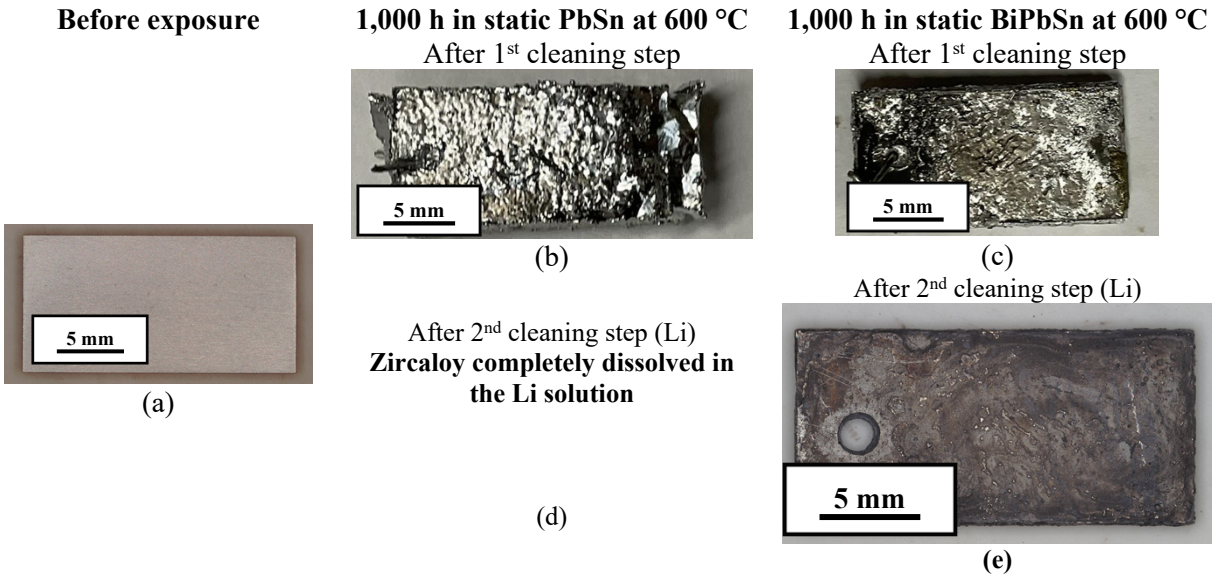

Figure 7. Keyence images of Zr4 specimen (a) before exposure, (b) after 1,000 h in static PbSn at 600 °C after the first cleaning step, (c) after 1,000 h in BiPbSn at 600 °C after the first cleaning step, (d) after 1,000 h in static PbSn at 600 °C after the second cleaning step in Li and (e) after 1,000 h in static BiPbSn at 600 °C after the second cleaning step in Li.

Figure 8 shows macroscopic images of the Zr4 specimens after 1,000 h of exposure to static tin, bismuth, and lead at 600 °C. The thickness of the Zr4 specimen exposed to liquid tin was at least two times larger than that before exposure (Figure 8a). The Zr4 specimen was significantly attacked by the liquid bismuth, such that only a small fraction of the specimen was recovered after exposure (Figure 8 b,e). Finally, limited macroscopic degradation of the Zr4 specimen was observed after exposure to static lead (Figure 8c and f).

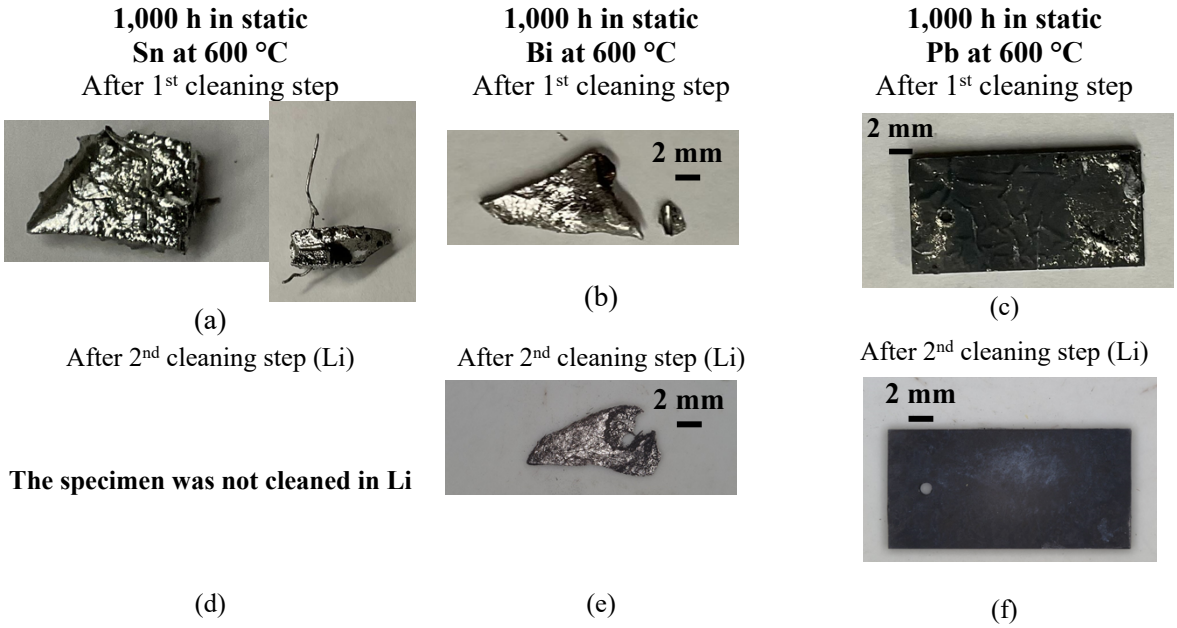

Figure 8. Keyence images of Zr4 specimen after exposure in (a) Sn, (b) Bi, and (c) Pb after the first cleaning step and (d) Sn, (e) Bi, and (f) Pb after the second cleaning step for 1,000 h at 600 °C .

2.2.4 Zircaloy-4 microstructure after exposure

Figure 9 shows BSE images of the Zr4 specimen before and after exposure to liquid tin at 600 °C and corresponding EDS linescan. After exposure, the Zr4 specimen was covered with 100% liquid tin (Figure 9) and completely transformed into Sn_2Zr intermetallic underneath, as identified by the EDS linescan (Figure 9b).

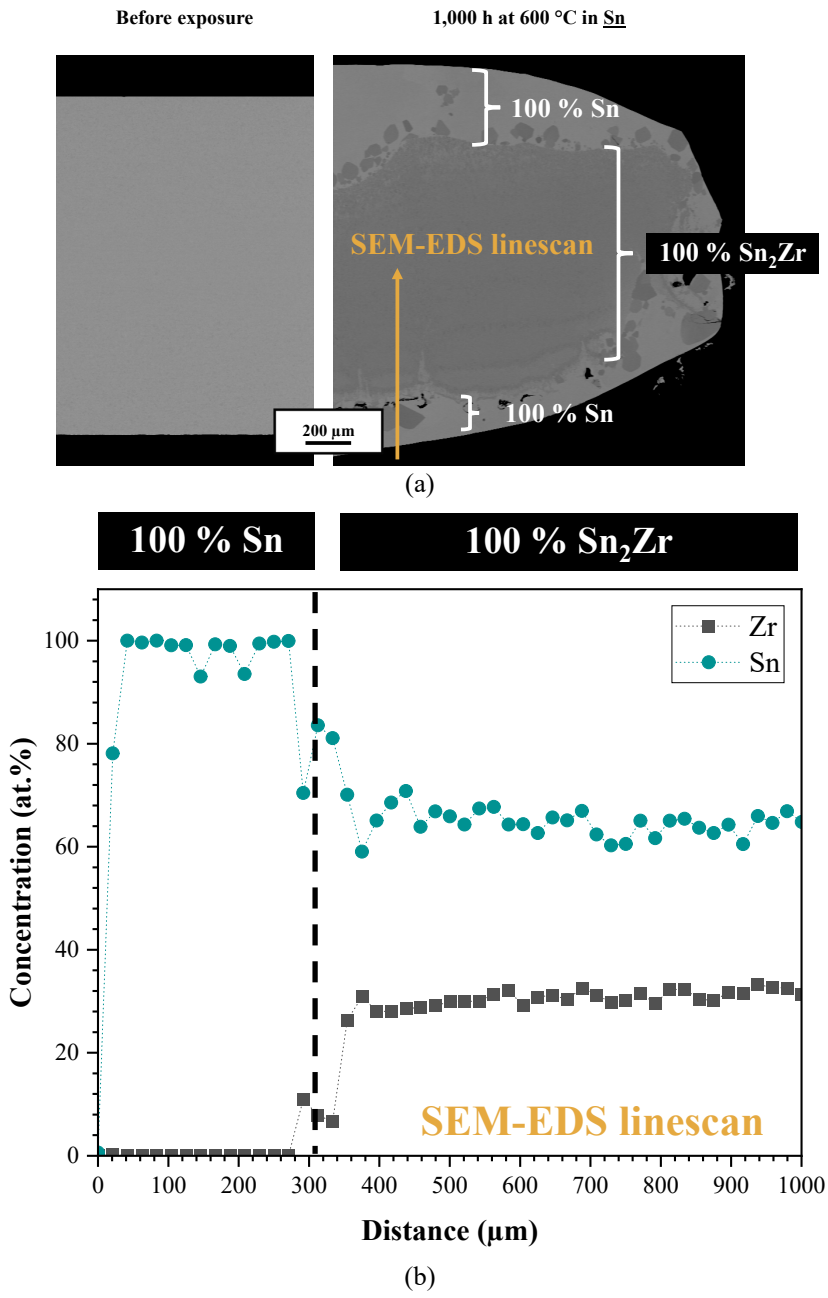

Figure 9. (a) BSE cross sections before and after exposure to liquid Sn for 1,000 h at 600 °C and (b) corresponding EDS linescan after exposure to liquid Sn.

Figure 10 shows that the Zr4 specimen almost completely reacted with the liquid bismuth to form (Bi, O)-rich zirconium compound surrounded by 100 % bismuth after 1,000 h at 600 °C. EDS point analyses measured 31 at.% O, 38 at.% Bi, and 31 at.% Zr within the (Bi, O)-rich zirconium compounds. In addition, image analysis (Figure 10) measured a specimen thickness of 313 ± 71 µm, which corresponded to a 80% reduction in specimen thickness after exposure.

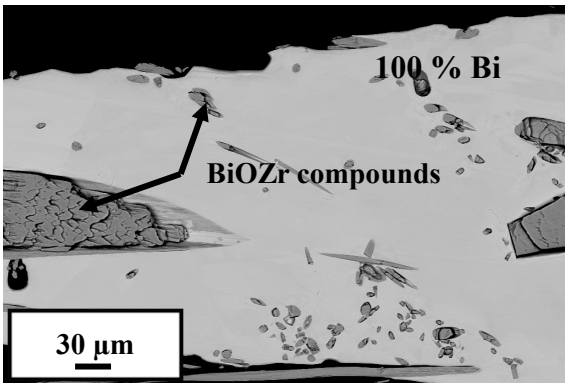

Figure 10. BSE image labeled using EDS point analysis of Zr4 specimen after 1,000 h of exposure in liquid Bi at 600 °C.

Figure 11 shows that the Zr4 specimens reacted with lead to form a (Pb, O)-rich zirconium layer of about 25 µm on the surface of the specimen after 1,000 h at 600 °C. In addition, an iron-rich layer (15 at.% Fe) was identified at the interface between the Zr4 specimen and the (Pb, O)-rich zirconium layer. Up to 10 at.% O was measured in the Zr4 specimen (Figure 11b).

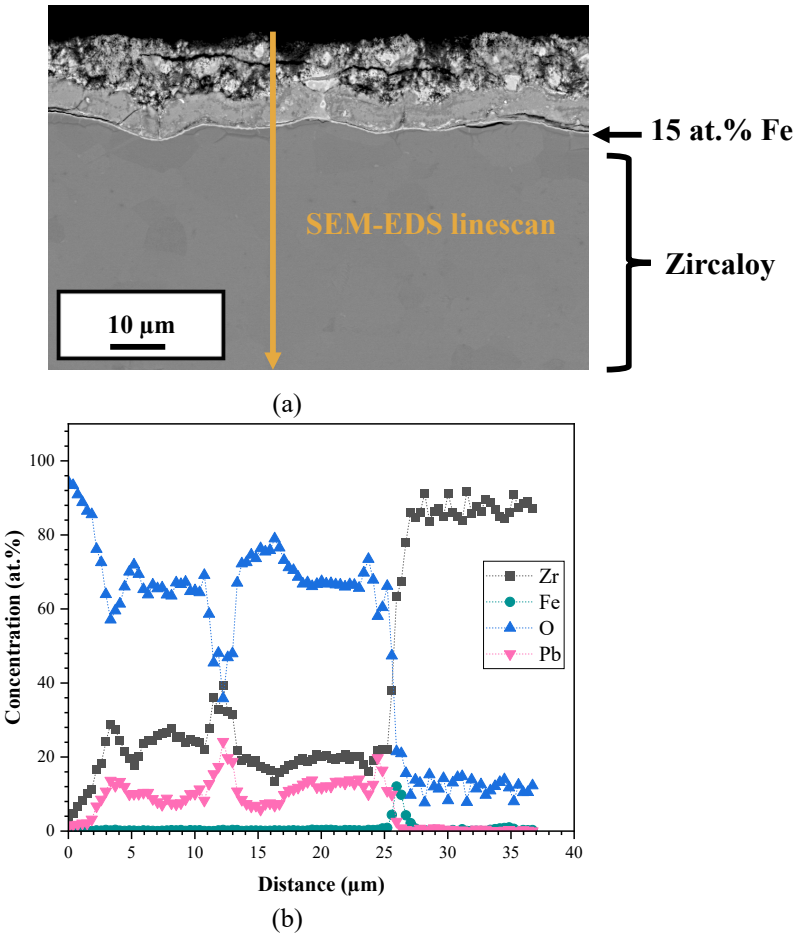

Figure 11. (a) BSE image and (b) corresponding EDS linescan of Zr4 specimen after 1,000 h of exposure in liquid Pb at 600 °C.

Figure 12 shows that an iron-rich layer (up to 18 at.%) of about 2 µm was formed on the surface of the Zr4 specimen after exposure to BiPbSn at 600 °C. Dissolution of zirconium was also observed along with the iron-rich layer, and about 10 at.% O was measured within the zirconium specimen (Figure 12b).

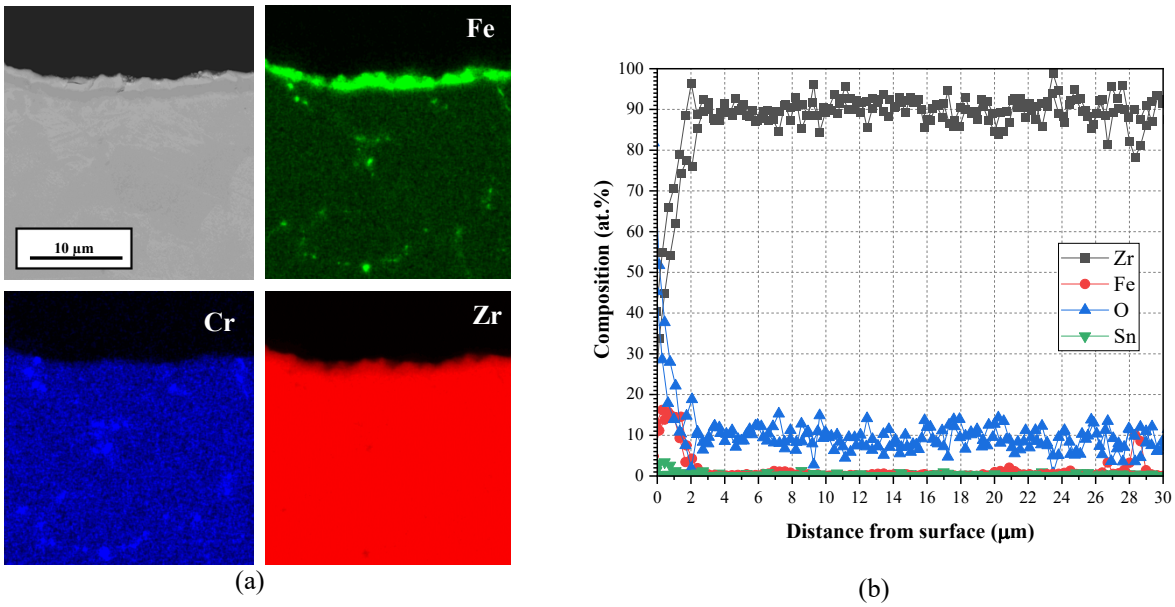

Figure 12. (a) EDS elemental maps and (b) EDS line scan of Zr4 specimen after 1,000 h in liquid BiPbSn at 600 °C.

2.3 DISCUSSION

Table 3 summarizes the reaction layer thicknesses documented in Section 2.2. Single-component liquid metals were tested only at 600°C. Bismuth and tin completely reacted with the Zr4 coupons, whereas lead had a 25 µm layer. PbSn and BiPbSn had identical reaction layer thicknesses at 400°C, but thicknesses were very different at 600°C. Whereas PbSn completely reacted with the Zr4, BiPbSn had only a 2 µm reaction layer.

Table 3. Summary of reaction layer thicknesses at 400°C and 600°C

Material	400°C	600°C
Bi	—	Complete
Pb	—	25 µm
Sn	—	Complete
PbSn	0.7 µm	Complete
BiPbSn	0.7 µm	2 µm

Thermodynamic phase diagrams provided insight into the observed reactions between Zr4 specimens and the various liquid metals. According to the zirconium–tin binary diagram [7], Sn_2Zr and $SnZr_4$ intermetallics are stable at 600 °C (Figure 13a), which is in agreement with the identification of Sn_2Zr intermetallic in Figure 9. The whole Zr4 specimen was transformed into the Sn_2Zr intermetallic, leaving no zirconium available to form the thermodynamically stable $SnZr_4$. Similarly, Bi_2Zr, BiZr, Bi_2Zr_3, Pb_3Zr_5, and $PbZr_4$ are thermodynamically stable at 600 °C (Figure 13 b,c) [8]. In addition, alpha zirconium can dissolve up to 30 at.% O in its matrix (Figure 13d) [9]. Therefore, the observation of (Bi, O)-rich and (Pb, O)-rich zirconium intermetallics is not surprising. Discerning the exact nature of the

intermetallics would require the use of surface x-ray diffraction, which could not be performed before the end of the project.

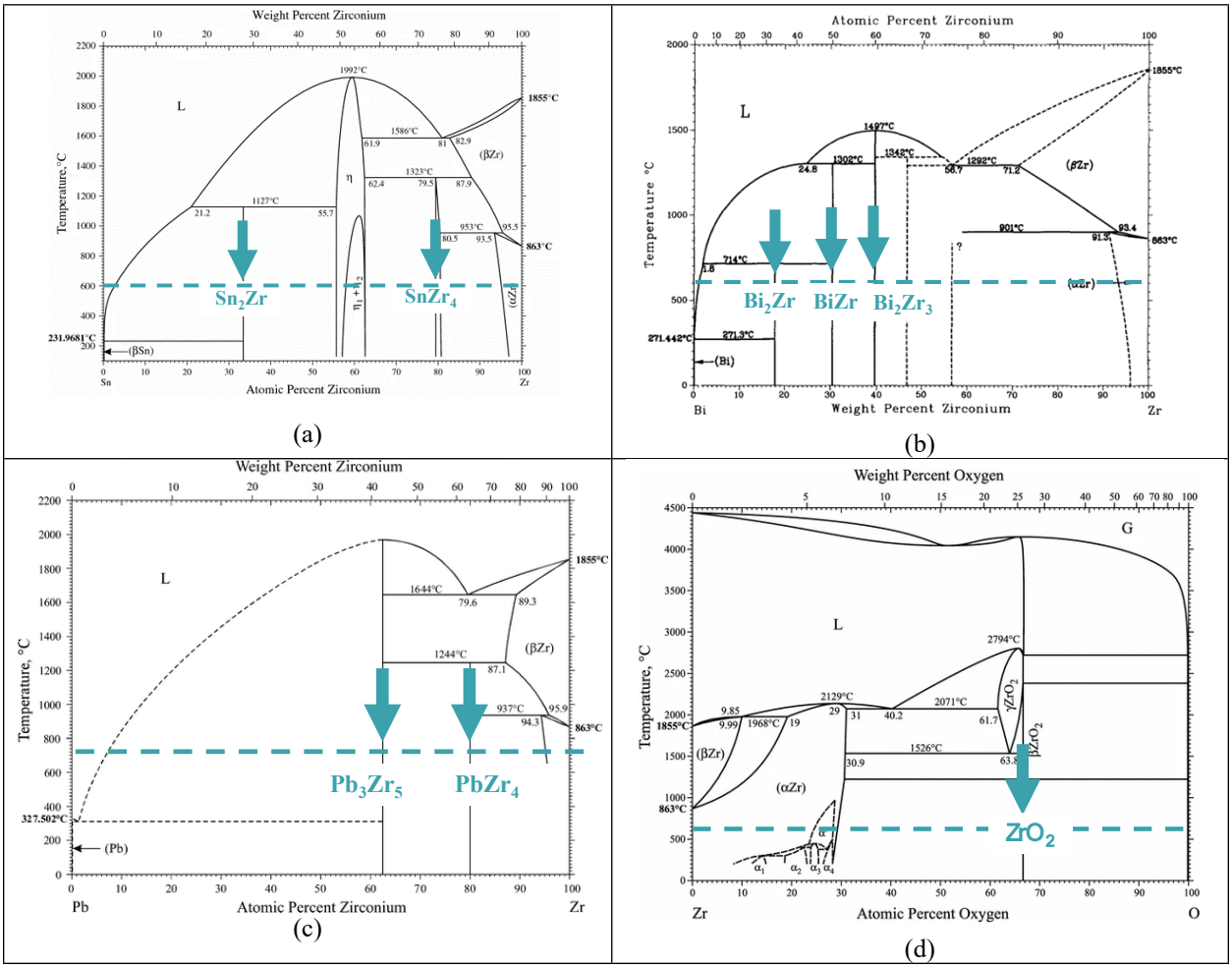

Figure 13. Binary phase diagrams (a) Zr-Sn, (b) Zr-Bi, (c) Zr-Pb, and (d) Zr-O binary phase diagrams [7–9].

Surprisingly, for both Zr4 specimens exposed for 1,000 h in lead and in BiPbSn at 600 °C, an iron-rich layer was observed at the oxide–alloy interface (Figure 11b and Figure 12). In the case of the specimen exposed in BiPbSn, the cleaning in liquid lithium most likely dissolved the oxide formed on the surface, and thus only the remaining underlying alloy was left to observe. As a reminder, the specimen exposed in lead did not require the second lithium cleaning step; thus, the (Pb, Zr)-rich oxygen layer could be observed.

Thermodynamic calculations were performed in ThermoCalc to understand the nature of the iron-rich phase at the alloy–oxide interfaces after 1,000 h exposure in lead and after 1,000 h in BiPbSn at 600 °C. This phase was not formed in the same conditions at 400 °C (Figure 5). According to the thermodynamic calculations shown in Figure 14, during oxygen ingress by the specimen and up to 10 at.%—which corresponded to the maximum oxygen content measured in the underlying specimens after exposure (Figures 11b and 12b)—the iron content in the Laves phase is predicted to decrease from 47 at.% to 45 at.%, whereas the chromium content is predicted to increase from 19 at.% to 21 at.% at 600 °C (Figure 15). However, the composition of the Laves phase is predicted to be stable at 400 °C in the presence of oxygen in the HCP matrix (Figure 15). These calculations suggest that the iron-rich phase observed at the

oxide–alloy interface at 600 °C corresponded to the change in the Laves phase composition, which became less rich in iron and released iron into the zirconium matrix. This is not predicted to occur at 400 °C, which was indeed not observed (Figure 5).

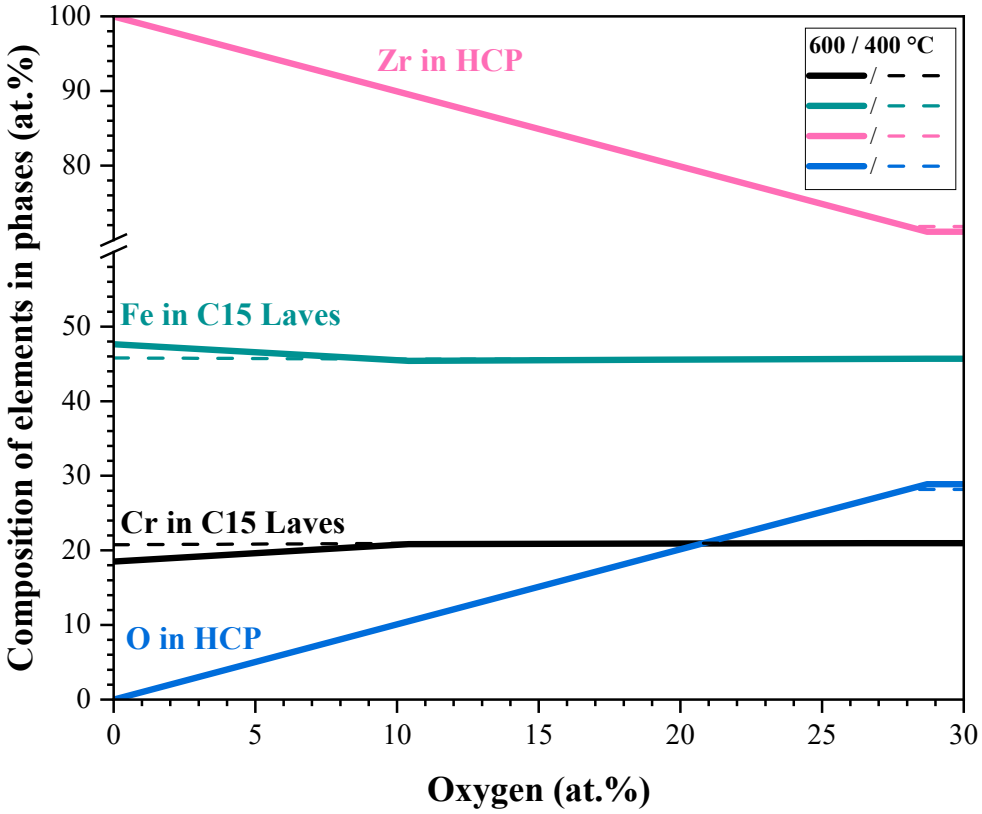

Figure 14. ThermoCalc calculations of elemental composition of HCP and Laves phases as a function of oxygen content in HCP at both temperatures of interest (400 and 600 °C) using the TCFE8 database.

3. DEPLETION SIMULATIONS

This simulation set uses the same reactor design as the previous scoping calculations [6], which is shown in Figure 15. It consists of a single vertical Zr4 pipe surrounded by the ULIMES fuel, which forms the core. Water is pumped through the pipe. The core is 2.5 m long. The water pipe extends 0.25 m beyond the inlet and outlet to reduce core leakage. The pipe has an interior radius of 25 mm, a wall thickness of 0.9 mm, and a 10 mm fuel region. This core was chosen both for simplicity and to evaluate water flow rate as a reactor control mechanism. To maintain LWR operating conditions, the Zr4 pipe wall should not exceed a peak temperature of 400°C. The fuel was modeled as a homogenous mixture of UO_2 and PbSn. BiPbSn cannot be modeled at this time because it has not been sufficiently characterized to accurately model the material.

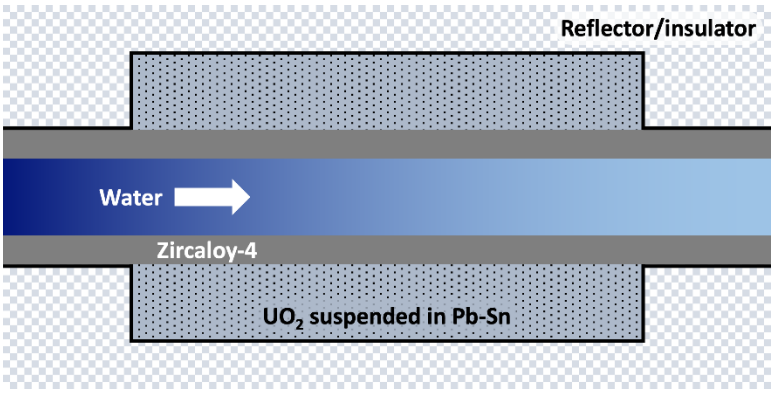

Figure 15. Diagram of simulation domain (not to scale). Modified from [6].

The original scoping calculations were not designed to measure burnup. Nevertheless, by using enrichment as a stand-in for depletion, it was estimated that the core modeled could achieve a burnup of 4.9 GWd·MTU^{-1}. This is significantly lower than the current Nuclear Regulatory Commission (NRC) limit of 62 GWd·MTU^{-1}. Such a low burnup is not conducive to economic reactor designs. Therefore, ULIMES is more likely to be a viable nuclear fuel if it can achieve a burnup of 62 GWd·MTU^{-1}without exceeding the 400°C pipe wall temperature limit.

3.1 SIMULATION DESIGN

The goal of the simulation was to calculate the depletion of the fuel given a set of reasonable design constraints:

- At each time step, the neutron multiplication factor (k) must be equal to one (pseudo-steady-state)
- The core-wide heat generation must be constant
- k should be maintained by adjusting the water flow rate
- The operating space would be defined by the core-wide heat generation and the weight fractions of UO_2 and Gd_2O_3 in the fuel

The main design differences between this study and the previous simulation are the calculation of fuel depletion over time, the inclusion of a burnable poison in the fuel (Gd_2O_3), and setting the power output to a specified value rather than the water flow rate.

The model consisted of four physics modules: OpenMC, MOOSE, IAPWS, and HT. OpenMC is an open-source Monte Carlo particle transport code [10]. It was used to model the reaction cross sections and track fuel depletion. MOOSE (Multiphysics Object-Oriented Simulation Environment) is an open-source finite element code maintained by Idaho National Laboratory [11]. It was used to model heat transport within the fuel and pipe wall regions of the simulation. IAPWS (International Association for the Properties of Water and Steam) is an international non-profit that publishes a highly accurate water model [12]. It was used to predict the water temperature, density, and vapor quality. HT is a Python package for calculating heat convection coefficients [13]. It was used to calculate the heat convection coefficient between the pipe wall and the water. The properties passed between these modules are diagramed in Figure 16. The simulation was written in Python, for which OpenMC, IAPWS, and HT have interfaces. Information was passed to and from MOOSE through CSV files. More information on each module is provided in Sections 3.1.1–3.1.4.

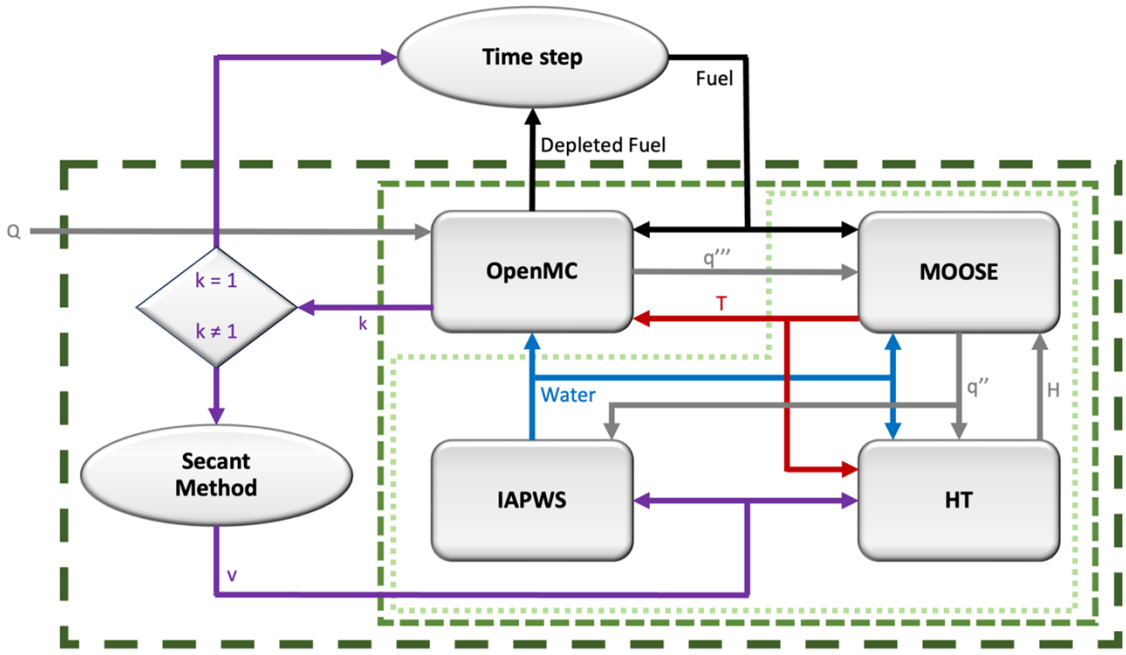

Figure 16. Simulation architecture. The four physics modules are shown as gray rectangles, with the information passed between them as solid lines. Dashed green boxes show the three levels of iterative solvers. Fuel refers to the ULIMES composition, H refers to the convection heat transfer coefficient ($W \cdot m^{-2} \cdot K^{-1}$), k is the neutron multiplication factor, Q is the overall heat generation rate (W), q'' is the heat flux between the pipe and water ($W \cdot m^{-2}$), q''' is the heat generation density ($W \cdot m^{-3}$), T is the fuel and pipe temperature profiles (K), v is the water inlet velocity ($m \cdot s^{-1}$), and Water refers to the water properties such as temperature, density, enthalpy, etc. Each time step is considered solved when $k = 1$. If $k \neq 1$, then the secant method is used to adjust the critical water inlet velocity.

Figure 16 also shows the various levels of iterative solvers employed in the model as dashed green boxes. The inner-most iteration loop solved the MOOSE, IAPWS, and HT modules. This iteration loop was considered solved when the heat flux vector residual fell below 10^{-5} $W \cdot m^{-2}$. Information from this solution was passed to the second iteration loop, which solved the OpenMC module. This scheme was used because the OpenMC module took significantly longer to run than the other modules. Solving the other modules before calling OpenMC reduced the number of OpenMC iterations and, therefore, the overall simulation time. This loop was considered converged when the heat generation vector residual was less than 0.07 $W \cdot m^{-3}$. The second loop tolerance had to be relatively loose because of the stochastic nature of OpenMC predictions.

Once all four physics modules were solved, the neutron multiplication factor (k) was used as the basis for determining whether the timestep reached pseudo-steady state and, therefore, whether the simulation could progress to the next timestep. The secant method was used to adjust the water inlet velocity (v) based on k until the condition $k - u \leq 1 \leq k + u$, where u was the uncertainty of k, was met. Note that u is automatically calculated by OpenMC. Timesteps were allowed to continue until either 360 days or v left a predefined range of acceptable velocities (0.7 $m \cdot s^{-1}$ to 35 $m \cdot s^{-1}$) without meeting the multiplication factor condition.

3.1.1 OpenMC

The OpenMC geometry consisted of one quarter of the water, pipe, and fuel regions of the core. OpenMC geometries consist of cells, each containing a unique material. The material properties of each cell were constant, so the fuel was split into 125 cells to account for changes in properties such as temperature and

density, whereas the water and pipe regions were split into 127 cells (125 plus inlet and outlet regions). The inlet and outlet had vacuum boundary conditions, which allowed neutrons to pass through and be lost. The remaining surfaces had reflective boundary conditions. Exterior reflective boundaries were used to suggest a reflector material was present, whereas interior reflective boundaries marked lines of symmetry. The domain and boundary conditions are shown in Figure 17. Note that the z-axis has been compressed for visibility.

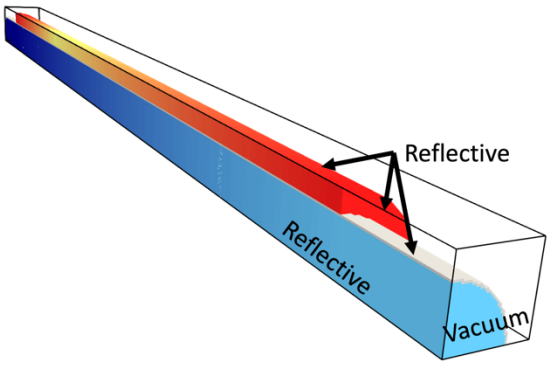

Figure 17. OpenMC simulation domain and boundary conditions. The water is shown in blue, the pipe in gray, and the fuel in red and yellow. The axial direction has been compressed for visibility.

Each timestep was solved as a steady-state calculation. This pseudo-steady-state approximation is valid because the timescale of neutron effects is orders of magnitude smaller than the timescale of other effects, such as depletion. The fission rate was calculated for each fuel cell, resulting in 125 depleted fuel compositions; however, these were averaged out to a uniform fuel composition between each timestep to approximate fuel flowing and mixing with time. Each OpenMC iteration used the same solving parameters: 100 batches with 1,000 particles and 10 inactive batches.

OpenMC was used to calculate the fission profile, heat generation density ($W \cdot m^{-3}$), neutron multiplication factor, and depleted fuel composition. The heat generation density was provided to MOOSE, while k was used in the solver and the fuel composition was used in the following timestep.

3.1.2 MOOSE

MOOSE's heat transport module was used to calculate heat generation and transfer between the fuel and pipe. The mesh was a 2D-RZ mesh generated by MOOSE's internal mesh system [11]. A convection boundary condition allowed heat to pass out of the mesh and into the water. The convection coefficient and water temperature were provided by the HT and IAPWS modules, respectively.

The system assumed stagnant fuel such that all heat transfer was due to conduction. This introduces some error but avoids making assumptions about fuel flow rate and movement of delayed neutron source terms. The heat conduction coefficients of the UO_2, PbSn, Zr4, and the fuel mixture were calculated in the same way as previous simulations [6]. MOOSE predicted the fuel and pipe wall temperatures as well as the heat flux, which was provided to the IAPWS module to predict the water properties.

3.1.3 IAPWS

The IAPWS water model calculates more than 60 water properties based on two inputs [12]. Allowable inputs include temperature, pressure, enthalpy, vapor quality, and others. For this work, the core was assumed adiabatic for simplicity, so a pressure of 7.17 MPa was always used as one of the inputs. The

inlet region's second input was temperature (489 K). Each of the 125 cells within the core used enthalpy as the second input by adding the heat flux from the pipe to the enthalpy of the water in the previous cell. All the other modules used the water properties. OpenMC used temperature and density to predict the moderation of the reaction, MOOSE used the temperature to calculate the heat flux, and HT used temperature and vapor quality to predict the heat transfer coefficient.

3.1.4 HT

The Python HT package calculated the convection heat transfer coefficient between the Zr4 pipe wall and the water. Two correlations were used: the *Nu_vertical_cylinder* class for single-phase flow and the Chen–Bennett correlation for two-phase flow. The convection coefficient was passed to MOOSE to calculate the heat flux.

3.2 LOW-ENRICHED URANIUM SIMULATION

The first depletion simulation was designed to use low-enriched uranium (LEU), which was enriched to 4.95% ^{235}U. The first step was to determine the optimum operating regime that would keep the peak pipe temperature below 400°C while maximizing the amount of uranium in the core. To identify the ideal operating regime, simulations were performed with fresh fuel throughout the potential operating domain. The results for a total heat generation rate of 2 MW are shown in Figure 18. Simulations using heat generation rates of 1.5 MW, 2.5 MW, 3 MW, 3.5 MW, and 4 MW were also performed but are not shown.

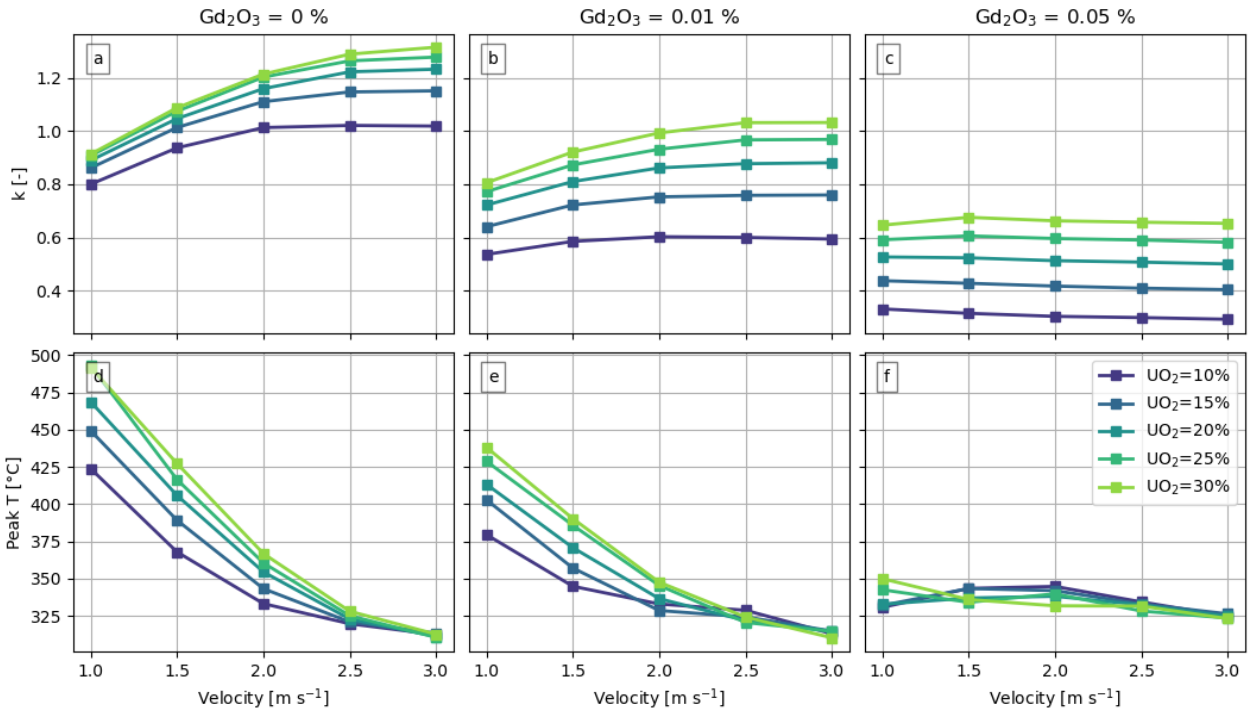

Figure 18. Neutron multiplication factor (a, b, c) and peak pipe temperature (d, e, f) predictions for fresh-fuel simulations with a reactor power of 2 MW. Five weight fractions of UO_2 (lines) are shown along with three Gd_2O_3 weight fractions (columns).

Figure 18 also shows an unexpected property of the reactor. The water inlet velocity is not always an effective control mechanism. Plot 18a shows that when the velocity is below 2 m·s^{-1}, increasing velocity likewise increases the neutron multiplication factor. However, when the velocity is greater than 2 m·s^{-1},

further increasing the velocity does nothing to the multiplication factor. This effect is even more pronounced in Plot 18c, which shows that increasing the velocity had a small negative effect on k. This limited the feasible operating regime, similar to the peak pipe temperature constraint.

Eventually, a set of conditions that led to acceptable temperatures and good control was identified: 2 MW power with a fuel composed of 20 wt% UO_2 and 0.02 wt% Gd_2O_3. These conditions were used in a depletion simulation that lasted 90 days. Figure 19 shows several time-dependent predictions, including the peak pipe temperature, water inlet velocity, water vapor quality, and burnup.

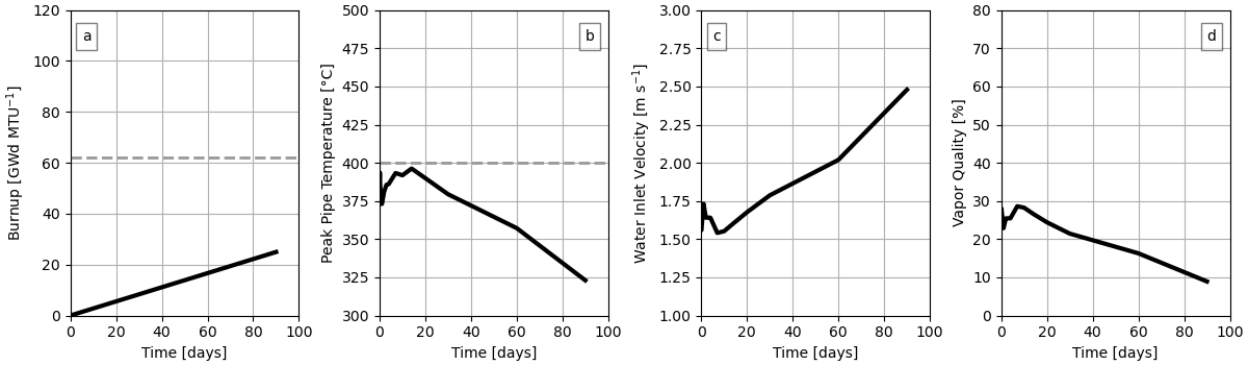

Figure 19. Time-dependent simulation predictions for the LEU case. a) burnup, b) peak pipe temperature, c) water inlet velocity, d) vapor quality. Horizontal dashed lines show the target burnup and maximum allowable temperature.

The heat generation rate was held constant by adjusting the water inlet velocity. Early in the core lifetime, the water inlet velocity had to be decreased, but after ~10 days, the velocity increased relatively uniformly. Throughout this time, the peak pipe temperature stayed below 400°C. The peak pipe temperature and vapor quality profiles were both mirror images of the water inlet velocity. The burnup accumulated at a rate of 277.4 MW·MTU^{-1}, resulting in a peak burnup of 25.0 GWd·MTU^{-1}.

Changes in the fuel composition with time are shown in Figure 20. The amount of ^{235}U decreased steadily from 0.47 at.% to 0.26 at.%. The amount of ^{238}U decreased slightly from 8.9 at.% to 8.8 at.%. This was primarily due to breeding of ^{239}Pu, which reached a concentration of 0.04%. Interestingly, despite being included as a burnable poison, the rate of gadolinium depletion was not matched by the rate of gadolinium generation as a fission product, so the amount of gadolinium in the fuel increased from 1.4×10^{-5} to 1.7×10^{-5}. Finally, the fission product poison reached a peak concentration of 1.2×10^{-7} after one day and then decreased slowly to 4.4×10^{-8}.

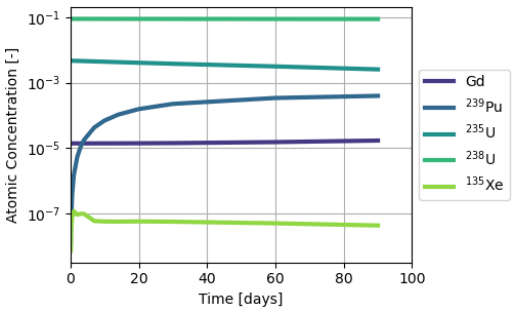

Figure 20. Atomic concentrations of several elements and isotopes of interest within the LEU ULIMES fuel as a function of time.

The axial profile of several parameters of interest are shown in Figure 21. The heat generation rate shows that the fission reaction initially occurs primarily at the core inlet, where the water density is highest. This corresponds to a large temperature spike and a sudden increase in the water vapor quality. As time progresses, the reaction becomes more diffuse, causing the temperature to fall and the water to begin boiling higher in the core. The outlet vapor quality falls because of the increase in the water flow rate over time.

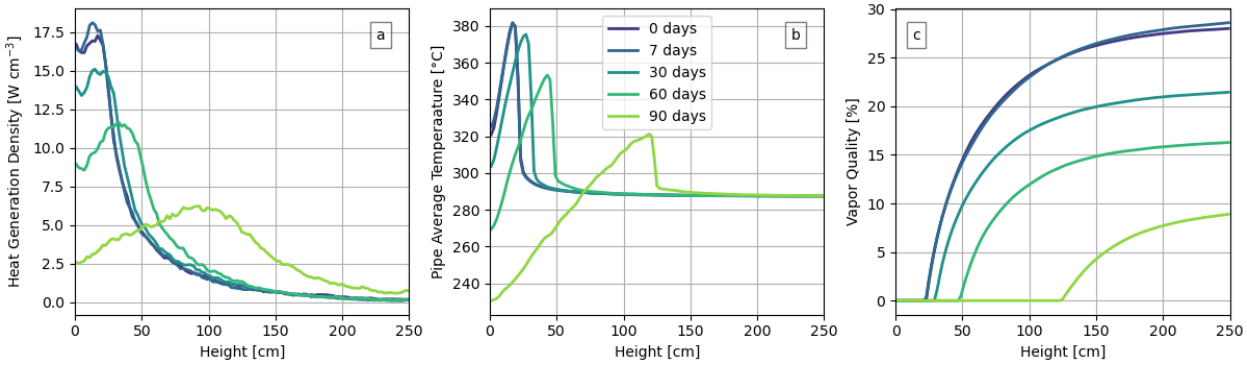

Figure 21. Changes of axial profiles of the a) heat generation density, b) pipe average temperature, and c) water vapor quality in the LEU case.

3.3 HIGH-ASSAY, LOW-ENRICHED URANIUM SIMULATION

Because no conditions could be found in which LEU fuel reached the target burnup, a second depletion simulation was run with high-assay LEU (HALEU). The ^{235}U was enriched to 19.5%, and operating space was specified as 3 MW of heat generation, 25 wt% UO_2, and 0.09 wt% Gd_2O_3. Figure 22 shows several time-dependent predictions of interest, including burnup, peak pipe temperature, water inlet velocity, and vapor quality. The burnup increased at a rate of 328 MW·MTU^{-1} for the entire 360 day simulation, resulting in a peak burnup of 118.2 GWd·MTU^{-1}, which is nearly double the target of 62 GWd·MTU^{-1}. The peak pipe temperature started at 399.7°C and then increased substantially to a peak of 489.3°C at 210 days. The water inlet velocity initially dropped but then began increasing relatively linearly from 1.2 m·s^{-1} to 2.9 m·s^{-1}. Changing the velocity caused the vapor quality to change in an inverse correlation. It peaked at 79% and went down to 18% after 360 days.

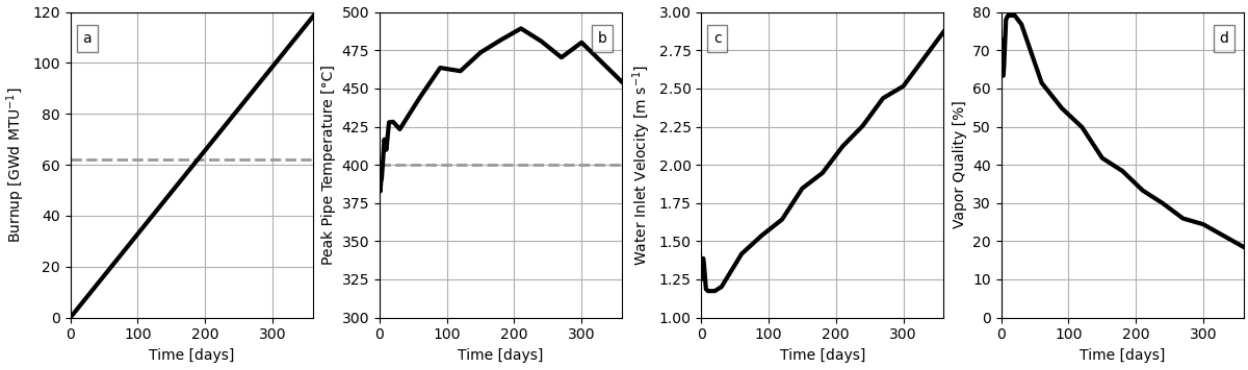

Figure 22. Time-dependent simulation predictions for the HALEU case. a) burnup, b) peak pipe temperature, c) water inlet velocity, d) vapor quality. Horizontal dashed lines show the target burnup and maximum allowable temperature.

Changes in the fuel composition over time are shown in Figure 23. The ^{235}U concentration decreased steadily from 2.3 at.% to 0.9 at.%. The ^{238}U concentration also decreased from 9.2 at.% to 8.6 at.%. This drop is related to the rise in ^{239}Pu, which reached a peak concentration of 0.17 at%. The gadolinium

concentration remained stable at 0.06 at.%. Finally, the ^{135}Xe concentration initially shot up to 8.3×10^{-7} at two days before dropping to 2.1×10^{-7}.

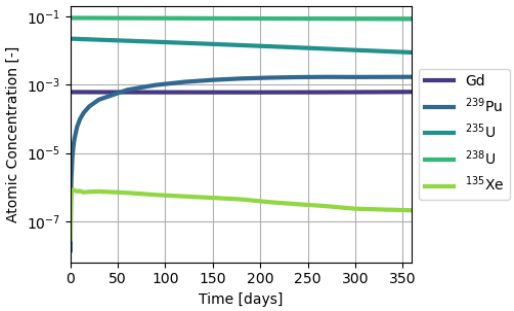

Figure 23. Atomic concentrations of several elements and isotopes of interest within the HALEU fuel as a function of time.

The axial profiles of several parameters of interest at several time steps are shown in Figure 24. Plot 24a shows the heat generation rate. As time progressed, the fission reaction became more concentrated at the core inlet. This behavior is opposite to that seen in Section 3.2. Plot 24b shows the effect of this concentration on the pipe temperature profile. The temperature at the core inlet increased to match the fission rate profile. Plot 24c shows the vapor quality. It decreased steadily with time, consistent with the trend shown in Figure 22.

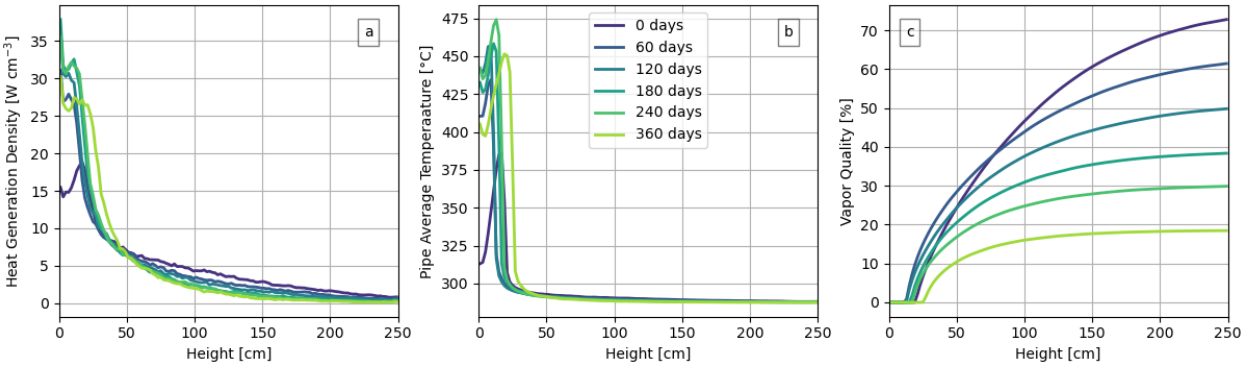

Figure 24. Changes of axial profiles of the a) heat generation density, b) pipe average temperature, and c) water vapor quality in the HALEU case.

3.4 10% ENRICHMENT

A second HALEU case was developed with a lower enrichment to attempt to find a middle ground between the two previous simulations. The operating regime was scoped out again for 10% enriched ^{235}U. The ideal condition with an initial peak pipe temperature below 400 °C and a strong correlation between reactivity and water velocity was identified as 2 MW of heat generation and fuel composed of 30 wt% UO_2 and 0.03 wt% Gd_2O_3. Time-dependent predictions are shown in Figure 25. The burnup rate was 180 MW·MTU^{-1}. This is lower than both other cases due to the increased concentration of UO_2 in the fuel. After 360 days, it reached a burnup of 64.7 GWd·MTU^{-1}.

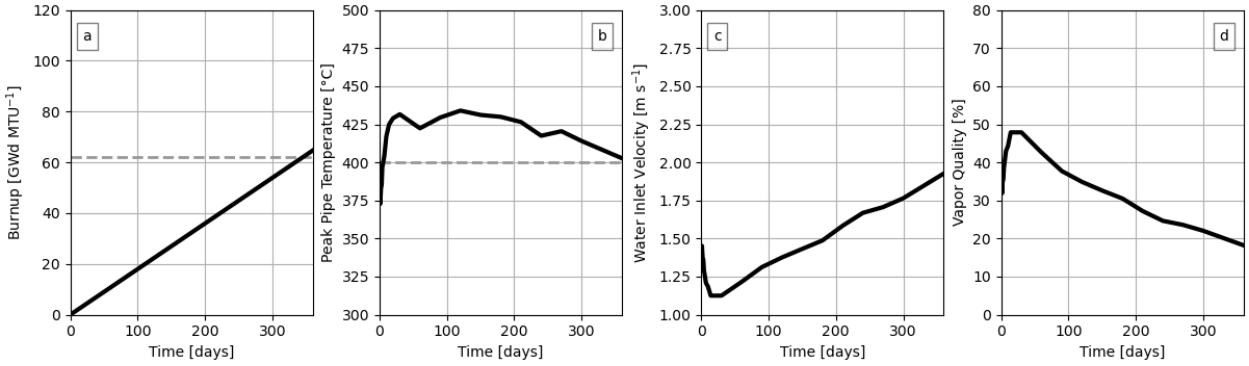

Figure 25. Time-dependent simulation predictions for the 10% enrichment case. a) burnup, b) peak pipe temperature, c) water inlet velocity, d) vapor quality. Horizontal dashed lines show the target burnup and maximum allowable temperature.

Like the HALEU case, the peak pipe temperature started within the 400°C limit (379.0°C), but quickly exceeded the limit and achieved a peak temperature of 434°C at 120 days. The water inlet velocity started at 1.39 $m \cdot s^{-1}$, decreased to 1.12 $m \cdot s^{-1}$ from days 14 to 30, then increased to 1.93 $m \cdot s^{-1}$. The water vapor quality started at 34.2%, increased to a peak of 47.9%, and then decreased to 18.2%. The changes in vapor quality were directly proportional to the water inlet velocity.

Figure 26 shows the concentrations of various components of the fuel. Uranium-235 began with a concentration of 1.4% and fell steadily to 0.6%. The amount of gadolinium was stable. It remained 0.02% for the entire simulation. Xenon-135 reached a maximum concentration of 3.15×10^{-7} before slowly decreasing to 1.06×10^{-7}.

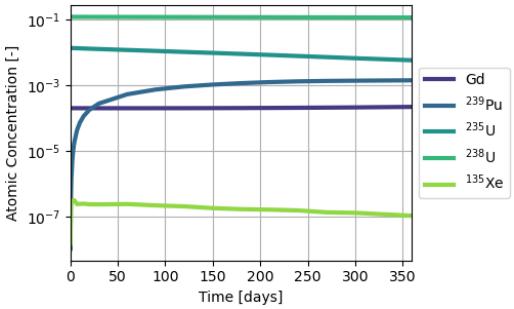

Figure 26. Atomic concentrations of several elements and isotopes of interest within the 10% enriched fuel as a function of time.

The axial profiles of several parameters at various times throughout the simulation are shown in Figure 27. The overall behavior of the system was similar to the HALEU case. The heat generation density spiked at the core inlet between 60 and 120 days before slowly decreasing. The temperature profile spiked similarly, causing the peak temperature rise seen in Figure 25.

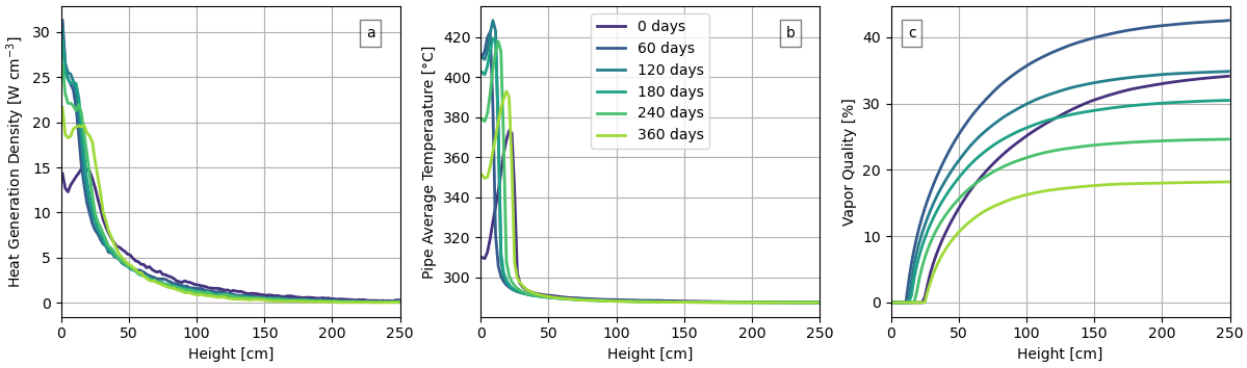

Figure 27. Changes of axial profiles of the a) heat generation density, b) pipe average temperature, and c) water vapor quality in the 10% enrichment case.

3.5 DISCUSSION

The purpose of these simulations was to optimize the burnup without exceeding a peak pipe temperature of 400 °C while maintaining a constant heat generation rate. The LEU case maintained the proper temperature but achieved a burnup of only 25 GWd·MTU^{-1}. The HALEU case, by contrast, exceeded the 400°C temperature limit, but achieved a burnup of 118 GWd·MTU^{-1}. A third simulation with 10% enriched ^{235}U behaved similarly to the HALEU case. It exceeded the temperature limit but achieved a burnup of 64.7 GWd·MTU^{-1}. Of course, the three operating conditions examined here were far from exhaustive. It is possible that another set of conditions would strike a better balance between peak burnup and peak pipe temperature. However, no such operating regime was found in the scoping calculations for LEU, HALEU, or 10% enriched cases.

The LEU simulation (Figure 19) also shows the fission reaction concentrating at the core inlet at the 7 day mark, but it had started to diffuse by the 30 day mark. Likewise, Figure 24 shows that after 240 days, the HALEU fission reaction also began to diffuse. The cause of this concentration to diffusion behavior pattern is unclear, except in that the relationship between fuel depletion and fission rate profile is non-linear.

4. CONCLUSIONS AND FUTURE WORK

A new fuel was recently proposed that consists of UO_2 particles suspended in a liquid metal. ULIMES fuel has a significantly higher thermal conductivity than that of sintered UO_2 pellets, potentially creating better conditions for passive cooling and moderator-based reactor control. A literature review identified two liquid metal candidates: BiPbSn and PbSn. In addition, preliminary scoping calculations showed that the fuel may have a limited burnup potential. The current work aimed to select the liquid metal most compatible with Zr4 and to gain additional insight into the burnup behavior of the fuel.

Liquid metal corrosion experiments were performed between Zr4 and Bi, Pb, Sn, PbSn, and BiPbSn. The literature suggests that bismuth and lead are excessively corrosive at around 400 °C, but BiPbSn forms a protective layer that self-limits the corrosion rate [14]. The literature also tested BiPbSn at 650 °C, and it was found that although the reaction was no longer self-limiting, the reaction rate was acceptably low [14].

In this work, BiPbSn and PbSn both had very limited reaction layers 0.7 µm) at 400°C, which corroborates the literature. At 600 °C, it was found that lead had a reaction layer of about 25 µm. Bismuth, tin, and PbSn completely reacted with the Zr4. But BiPbSn had a reaction layer of 2µm. The

extent to which these results corroborate or conflict with those found in the literature is not completely clear without reaction rate data. However, it is clear that of all the alloys tested, BiPbSn was the least reactive with Zr4 at both temperatures. Moreover, alternative pipe materials such as FeCrAl were not examined as part of this work and may be compatible with different liquid metal mixtures.

The scoping calculations from previous work [6] were modified to include fuel depletion so that accurate burnup predictions could be made. Similar to the original work, a tradeoff between achievable burnup and core temperature was identified. LEU fuel stayed within the LWR temperature range but achieved a peak average burnup less than half that of currently operating reactors. HALEU fuel could achieve a burnup that matches or exceeds current reactor limits, but the core temperature exceeds the standard temperature limits of Zr4.

These results suggest that the next steps for ULIMES development include measuring BiPbSn and ULIMES material properties such as thermal conductivity, density, viscosity, and particle settling rate. These properties are currently unknown and will be important base properties for any reactor designs that utilize this fuel. In addition, more realistic reactor core designs should be investigated to identify methods that mitigate the peak operating temperature, maximize passive cooling while the reactor is shut down, and minimize operating costs. The results shown here suggest that some additional controls beyond water flow rate may be needed to reduce the operating temperature and ensure safe operation in accident conditions.

ACKNOWLEDGMENTS

The authors sincerely thank M. Stephens, B. Johnston, A. Willoughby, C. De Lamater-Brotherton, D. Sulejmanovic, Tracie Lowe, Y. F. Su, D. Newberry for their help with the experimental work and C. Massey for providing the Zr4 specimens. The Nuclear Nonproliferation Division is acknowledged for providing access to the Zeiss Gemini 460 SEM. This research sponsored by the Laboratory Directed Research and development program (LDRD) SEED money fund.

5. REFERENCES

[1] Annual Energy Outlook 2023, U.S. Energy Information Administration, Washington, DC, 2023. https://www.eia.gov/outlooks/aeo/ (accessed January 17, 2024).
[2] New Alloy Material Approved for Use in High-Temperature Nuclear Plants, Energy.Gov (2020). https://www.energy.gov/ne/articles/new-alloy-material-approved-use-high-temperature-nuclear-plants (accessed November 30, 2021).
[3] G.L. Beausoleil, C. Petrie, W. Williams, A. Jokisaari, L. Capriotti, S. Novascone, C. Adkins, M. Kerr, Integrating Advanced Modeling and Accelerated Testing for a Modernized Fuel Qualification Paradigm, Nucl. Technol. 207 (2021) 1491–1510. https://doi.org/10.1080/00295450.2020.1826272.
[4] Keeping Up with the Advanced Nuclear Industry – Third Way, (n.d.). https://www.thirdway.org/graphic/keeping-up-with-the-advanced-nuclear-industry (accessed December 5, 2019).
[5] J.K. Shultis, R.E. Faw, Fundamentals of Nuclear Science and Engineering, Second Edition, CRC Press, Boca Raton, Florida, 2008.
[6] I. Greenquist, UO2-liquid metal suspension fuel concept for enhanced passive safety of LWRs: A heat pipe case study, Nucl. Eng. Des. 398 (2022) 11. https://doi.org/10.1016/j.nucengdes.2022.111972.
[7] H. Okamoto, Sn-Zr (Tin-Zirconium), J. Phase Equilibria Diffus. 31 (2010) 411–412. https://doi.org/10.1007/s11669-010-9734-4.

[8] H. Okamoto, Pb-Zr (Lead-Zirconium), J. Phase Equilibria Diffus. 32 (2011) 568–569. https://doi.org/10.1007/s11669-011-9953-3.
[9] H. Okamoto, O-Zr (Oxygen-Zirconium), J. Phase Equilibria Diffus. 28 (2007) 498–498. https://doi.org/10.1007/s11669-007-9154-2.
[10] P.K. Romano, N.E. Horelik, B.R. Herman, A.G. Nelson, B. Forget, K. Smith, OpenMC: A state-of-the-art Monte Carlo code for research and development, Ann. Nucl. Energy 82 (2015) 90–97. https://doi.org/10.1016/j.anucene.2014.07.048.
[11] R.C. Martineau, The MOOSE Multiphysics Computational Framework for Nuclear Power Applications: A Special Issue of Nuclear Technology, Nucl. Technol. 207 (2021) iii–viii. https://doi.org/10.1080/00295450.2021.1915487.
[12] W. Wagner, A. Pruß, The IAPWS Formulation 1995 for the Thermodynamic Properties of Ordinary Water Substance for General and Scientific Use, J. Phys. Chem. Ref. Data 31 (2002) 387–535. https://doi.org/10.1063/1.1461829.
[13] C. Bell, Contributors, ht: Heat transfer component of Chemical Engineering Design Library, (n.d.). https://github.com/CalebBell/ht.
[14] R.F. Wright, J.S. Tulenko, G.J. Schoessow, R.G.C. Jr, M.A. Dubecky, T. Adams, Thermal Bonding of Light Water Reactor Fuel Using Nonalkaline Liquid-Metal Alloy, Nucl. Technol. 115 (1996) 281–292. https://doi.org/10.13182/NT96-A15838.